The Astronomical Journal, 169:239 (10pp), 2025 May https://doi.org/10.3847/1538-3881/adbe75
© 2025. The Author(s). Published by the American Astronomical Society.
OPEN ACCESS

Low 4.5 μm Dayside Emission Disfavors a Dark Bare-rock Scenario for the Hot Super-Earth TOI-431 b

Christopher Monaghan[1], Pierre-Alexis Roy[1], Björn Benneke[1,2], Ian J. M. Crossfield[3,4], Louis-Philippe Coulombe[1], Caroline Piaulet-Ghorayeb[1,5], Laura Kreidberg[4], Courtney D. Dressing[6], Stephen R. Kane[7], Diana Dragomir[8], Michael W. Werner[9], Vivien Parmentier[10], Jessie L. Christiansen[11], Farisa Y. Morales[9], David Berardo[12,13], and Varoujan Gorjian[9]

[1] Department of Physics and Trottier Institute for Research on Exoplanets, Université de Montréal, Montreal, QC H3C 3J7, Canada; christopher.monaghan@umontreal.ca
[2] Department of Earth, Planetary, and Space Sciences, University of California, Los Angeles, Los Angeles, CA, USA
[3] Department of Physics and Astronomy, University of Kansas, Lawrence, KS 66045, USA
[4] Max Planck Institut für Astronomie, Königstuhl 17, 69117, Heidelberg, Germany
[5] Department of Astronomy & Astrophysics, University of Chicago, 5640 South Ellis Avenue, Chicago, IL 60637, USA
[6] Department of Astronomy, University of California, Berkeley, CA 94720, USA
[7] Department of Earth and Planetary Sciences, University of California, Riverside, CA 92521, USA
[8] Department of Physics and Astronomy, University of New Mexico, Albuquerque, NM 87106, USA
[9] Jet Propulsion Laboratory, California Institute of Technology, 4800 Oak Grove Drive, Pasadena, CA 91109, USA
[10] Atmospheric, Oceanic & Planetary Physics, Department of Physics, University of Oxford, Oxford, OX1 3PU, UK
[11] Caltech/IPAC-NExScI, M/S 100-22, 1200 E. California Boulevard, Pasadena, CA 91125, USA
[12] Department of Earth, Atmospheric and Planetary Sciences, Massachusetts Institute of Technology, Cambridge, MA 02139, USA
[13] Department of Physics and Kavli Institute for Astrophysics and Space Research, Massachusetts Institute of Technology, Cambridge, MA 02139, USA
Received 2024 December 18; revised 2025 February 21; accepted 2025 March 7; published 2025 April 2

Abstract

The full range of conditions under which rocky planets can host atmospheres remains poorly understood, especially in the regime of close-in orbits around late-type stars. One way to assess the presence of atmospheres on rocky exoplanets is to measure their dayside emission as they are eclipsed by their host stars. Here, we present Spitzer observations of the 4.5 μm secondary eclipses of the rocky super-Earth TOI-431 b, whose mass and radius indicate an Earth-like bulk composition ($3.07 \pm 0.35\,M_\oplus$, $1.28 \pm 0.04\,R_\oplus$). Exposed to more than 2000 times the irradiation of Earth, dayside temperatures of up to 2400 K are expected if the planet is a dark bare rock without a significant atmosphere. Intriguingly, despite the strong stellar insolation, we measure a secondary-eclipse depth of only 33 ± 22 ppm, which corresponds to a dayside brightness temperature of 1520^{+360}_{-390} K. This notably low eclipse depth disagrees with the dark bare-rock scenario at the 2.5σ level, and suggests either that the planet is surrounded by an atmosphere or that it is a bare rock with a highly reflective surface. In the atmosphere scenario, the low dayside emission implies the efficient redistribution of heat to the nightside, or by molecular absorption in the 4–5 μm bandpass. In the bare-rock scenario, a surface composition made of a high-albedo mineral species such as ultramafic rock can lead to reduced thermal emission consistent with low eclipse depth measurement. Follow-up spectroscopic observations with the James Webb Space Telescope hold the key to constraining the nature of the planet.

Unified Astronomy Thesaurus concepts: Exoplanets (498); Exoplanet atmospheres (487); Planetary atmospheres (1244); Extrasolar rocky planets (511); Super Earths (1655)

1. Introduction

The ability for rocky exoplanets to retain sizable atmospheres under different conditions remains a key area of research. Although rocky planets are unlikely to retain their primordial hydrogen envelope, they may generate secondary atmospheres at later stages in their life (E. S. Kite & M. N. Barnett 2020; M. Tian & K. Heng 2024). Determining which rocky exoplanets host atmospheres and studying their properties will allow us to investigate how these atmospheric phenomena impact planetary evolution.

A number of processes are known to affect the atmospheric retention of exoplanets. Mass loss is driven by many factors, including photoevaporation and stellar wind erosion caused by high levels of irradiation from the host star (e.g., D. Kubyshkina 2024). Core-powered mass loss can also play a role after formation (S. Ginzburg et al. 2016, 2018). The age of the planet is also a key factor in determining an atmospheric presence, as older planets (>6 Gyr) may have ceased degassing processes, halting atmospheric replenishment (e.g., C. T. Unterborn et al. 2022).

The compositions of secondary atmospheres may impact the rate of atmospheric mass loss. For example, the initial content of volatiles in the star-forming region and associated protoplanetary disk will allow for the capture of gaseous species during the planet's evolution (R. Wordsworth & L. Kreidberg 2022). Furthermore, volcanism is known to affect the composition of planetary atmospheres through the outgassing of interior volatiles (P. Liggins et al. 2022, 2023). Studying the ways in which these processes interact is critical to understanding the conditions for atmospheric retention.

Detecting the atmospheres of warm exoplanets is readily achieved using thermal emission spectroscopy, which provides the most promising method to constrain the surface

Original content from this work may be used under the terms of the Creative Commons Attribution 4.0 licence. Any further distribution of this work must maintain attribution to the author(s) and the title of the work, journal citation and DOI.

composition of rocky planets (R. Alonso 2018; E. A. Whittaker et al. 2022). Such studies require distinguishing the contribution of the exoplanet's light from the combined system during the planet's secondary eclipse. Observing the occultations and phase curves of rocky planets in the infrared regime allows us to detect the presence of an atmosphere by measuring the brightness temperature of the planet (D. D. B. Koll et al. 2019). These observations are especially favorable for hot exoplanets orbiting late-type stars as the higher dayside temperatures result in larger eclipse depths.

1.1. Thermal Emission Spectroscopy of Terrestrial Bodies

Discovering which rocky exoplanets have atmospheres will further our understanding of the factors causing atmospheric loss and retention on terrestrial bodies. Close-in terrestrial planets are more susceptible to atmospheric loss due to the high irradiation received from their host stars, and are unlikely to host a significant gaseous envelope (E. D. Lopez 2017). However, highly irradiated hot planets may host molten surfaces, which could maintain volatile-rich atmospheres from the outgassing of lava (e.g., R. Hu et al. 2024; J. A. Patel et al. 2024). Particularly hot planets may instead host silicate atmospheres through the evaporation of surface magma (e.g., L. Schaefer & B. Fegley 2009; M. Maurice et al. 2024).

The present-day catalog of eclipse observations of rocky planets has produced a diverse range of results, and enforces the need for further research into how terrestrial planets develop and retain secondary atmospheres. Many planets observed fall into the subclass of ultra-short-period (USP) planets with orbital periods shorter than 1 day (R. Sanchis-Ojeda et al. 2014; J. N. Winn et al. 2018). One of the most well-studied USPs, 55 Cnc e, has been central to a number of emission-based studies in the infrared regime (e.g., B.-O. Demory et al. 2015; A. Tsiaras et al. 2016; K. C. Rasmussen et al. 2023; J. A. Patel et al. 2024). Recent observations by the James Webb Space Telescope (JWST) suggest that 55 Cnc e has a volatile-rich atmosphere comprised mostly of CO_2 or CO fueled by the outgassing of a magma ocean (R. Hu et al. 2024; J. A. Patel et al. 2024). K2 and Spitzer phase-curve observations of another USP planet, K2-141 b, have previously suggested the presence of a tenuous rock vapor atmosphere caused by a molten dayside (S. Zieba et al. 2022). In contrast, Spitzer observations of the USP planets LHS 3844 b and GJ 1252 b have shown these planets to have thermal emissions that are largely consistent with bare rocks without an atmosphere (L. Kreidberg et al. 2019; S. R. Kane et al. 2020; I. J. M. Crossfield et al. 2022). Similarly, JWST observations of a number of Earth-sized planets have found a lack of significant evidence for an atmospheric presence over a large range of dayside temperatures (T. P. Greene et al. 2023; S. Zieba et al. 2023; E. Ducrot et al. 2024; R. Luque et al. 2024; M. W. Mansfield et al. 2024; P. Wachiraphan et al. 2024; Q. Xue et al. 2024; M. Zhang et al. 2024). Recent studies of the super-Earth LHS 1478 b, however, observed a notably low eclipse depth, inconsistent with a bare-rock model (P. C. August et al. 2025). Thus, while the majority of terrestrial exoplanets observed so far are consistent with bare rocks, the reasons why some may be able to retain a secondary atmosphere remain largely unknown.

Table 1
Summary of Stellar and Planetary Parameters of TOI-431 b, with Error Bars

Parameter	Unit	Value	References
Stellar Parameters			
Stellar mass M_*	$M_\odot$	0.78 ± 0.07	(1)
Stellar radius R_*	$R_\odot$	0.731 ± 0.022	(1)
Effective temp. $T_{\rm eff}$	K	4850 ± 75	(1)
Planetary Parameters			
Mass M_p	$M_\oplus$	3.07 ± 0.35	(1)
Radius R_p	$R_\oplus$	1.28 ± 0.04	(1)
Bulk density ρ	g cm^{-3}	8.0 ± 1.0	(1)
Equilibrium temp. $T_{\rm eq}$	K	1862 ± 42	(1)
Max dayside temp. $T_{\rm d,max}$	K	2400 ± 60	(2)
Period P	day	$0.490\,047^{+0.000\,010}_{-0.000\,007}$	(1)
Semimajor axis a	au	$0.0113^{+0.0002}_{-0.0003}$	(1)
Impact parameter b		$0.34^{+0.07}_{-0.06}$	(1)
Scaled semimajor axis		3.324 ± 0.13	(2)
Transit time t_0	$\rm BJD_{TDB}$	$2458627.538^{+0.003}_{-0.002}$	(1)
Secondary eclipse $t_{\rm sec}$	$\rm BJD_{TDB}$	$2458627.783^{+0.003}_{-0.002}$	(2)

References. (1) A. Osborn et al. (2021), (2) This work, derived.

1.2. TOI-431 b

The USP super-Earth TOI-431 b is a prime target for infrared thermal emission measurements. The planet has a mass of $3.07 \pm 0.35\ M_\oplus$, a radius of $1.28 \pm 0.04\ R_\oplus$, and a period of 0.49 days (see Table 1; A. Osborn et al. 2021). TOI-431 b has an emission spectroscopy metric (ESM; E. M.-R. Kempton et al. 2018) of approximately 16 and orbits a cool K-type star, suggesting the potential for significant flux ratios to be measured during an occultation event (B. J. Hord et al. 2024).

TOI-431 b is expected to lack an atmospheric presence, as X-ray and ultraviolet (XUV) irradiation from the host star should drive an incredibly high mass-loss rate due to the close-in orbit (G. W. King et al. 2024; X. Jiang et al. 2025). Assuming a molten surface is present, recent simulations of TOI-431 b's emission spectra suggest an eclipse depth between 95 and 120 ppm to be measured at 4.5 μm, depending on the planet's surface temperature (F. L. Seidler et al. 2024). A similarly high eclipse depth is expected if the planet is consistent with a dark bare rock.

TOI-431 b was discovered orbiting a K-type star alongside the sub-Neptune TOI-431 d in 2021 by A. Osborn et al. (2021) using transit observations from the Transiting Exoplanet Survey Satellite (TESS; G. R. Ricker et al. 2014). A third nontransiting planet, TOI-431 c, was also discovered by A. Osborn et al. (2021) using high-precision Doppler spectroscopy from the High Accuracy Radial velocity Planet Searcher (F. Pepe et al. 2002) and the HIgh REsolution Spectrograph (S. S. Vogt et al. 1994). The system may serve as a key target in future studies of planetary evolution due to its unique orbital configuration, having one nontransiting planet between two transiting planets. Furthermore, TOI-431 b and TOI-431 d orbit on opposing sides of the radius–period valley, providing a rare opportunity to study the dichotomy between the evolution of planets in the same system on opposite ends of the gap (e.g., B. J. Fulton et al. 2017).

Here, we present Spitzer eclipse observations of the USP super-Earth TOI-431 b, combined with an analysis of the planet's potential atmosphere. In Section 2, we describe our analysis of the Spitzer observations and measure the eclipse

Table 2
Summary of Spitzer/IRAC 4.5 μm Visits and Measured Eclipse Depths and σ Error Bars as Calculated from the Pixel-level Decorrelation Reduction in ExoTEP

AOR	Date (YYYY-MM-DD)	Eclipse Depth (ppm)	Error $\pm$ σ (ppm)
69969664	2019-07-09	59	57
69969408	2019-07-19	105	59
69969152	2020-01-03	37	59
69968896	2020-01-06	-71	63
69968640	2020-01-07	51	57
69968128	2020-01-08	8	56
69967104	2020-01-09	28	56
Weighted average		**33**	**22**

depth and dayside brightness temperature of TOI-431 b. Section 3 discusses these measurements and compares the results to both bare-rock and atmospheric models of different compositions. The significance of our occultation depth and the results of our modeling are further discussed in Section 4. Finally, in Section 5, we present an analysis of TOI-431 b in the context of other thermal emission observations of rocky exoplanets, and consider future prospects of emission spectroscopy.

2. Observations and Data Reduction

2.1. Eclipse Observations

A total of seven eclipses of TOI-431 b were observed at 4.5 μm using the Spitzer Space Telescope Infrared Array Camera (IRAC) in Channel 2. These observations were taken as part of the large TESS planets follow-up program (GO 14084; I. Crossfield et al. 2018). We targeted this planet specifically because it was one of the highest-ESM rocky planets known while Spitzer was still operating. Two of these events were observed in 2019 July, while the remaining five were taken in 2020 January, shortly before Spitzer was decommissioned. Each observation was a continuous and near-identical exposure of ~5.24 hr centered approximately on the center of the predicted time of the secondary eclipse, allowing for ~2 hr of both pre-eclipse and post-eclipse baseline.

The Spitzer/IRAC images were processed using standard methods outlined in B. Benneke et al. (2017) and B. Benneke et al. (2019b). We start from the flat-fielded and dark-subtracted "Basic Calibrated Data" images, before using the method outlined in J. A. Kammer et al. (2015) for background subtraction. The position of the star is determined using flux-weighted centroiding with a radius of 3.5 pixels (B. Benneke et al. 2019a). The aperture, trim duration, and bin size are then chosen to minimize the rms of the unbinned residuals. The seven observations and their results from the following data analysis are summarized in Table 2.

2.2. Data Analysis

We analyzed the Spitzer light curves using the modular Exoplanet Transits Eclipses and Phasecurves (ExoTEP) framework (e.g., B. Benneke et al. 2017, 2019b, 2019a, 2024; P.-A. Roy et al. 2022, 2023; C. Piaulet-Ghorayeb et al. 2024). ExoTEP employs a Markov Chain Monte Carlo (MCMC) algorithm to fit the secondary-eclipse light curve and both

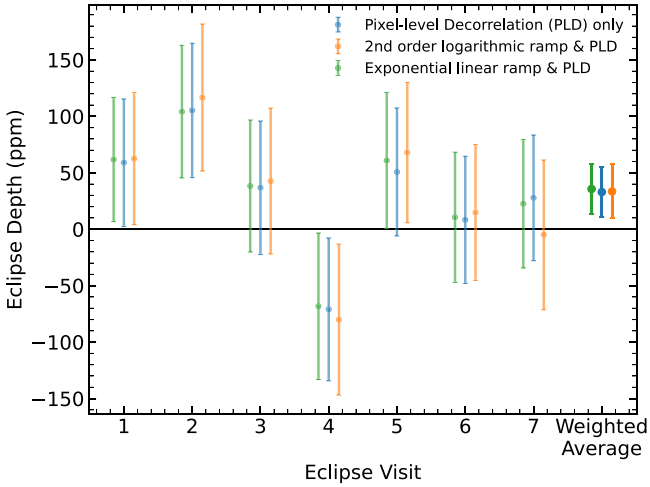

Figure 1. Measured eclipse depths for all seven visits using three different systematic models, including the associated error bars of each. The rightmost points show the weighted average across all visits for the individual systematics.

astrophysical and systematic parameters to the observed data. The emcee Python package was used to explore the joint posterior distributions of the parameters from uniform priors using the MCMC (D. Foreman-Mackey et al. 2013). For each visit, we perform an individual MCMC with 50,000 steps to fit the eclipse depth, photometric scatter, and systematic parameters. The remaining astrophysical parameters were set to values from A. Osborn et al. (2021). Given that the eccentricity of TOI-431 b is consistent with zero (A. Osborn et al. 2021), we do not fit for the time of the secondary eclipse, and instead use a value of $T_{\rm sec} = T_t + \frac{1}{2}P$ for all seven visits.

Considering TOI-431 b's short orbit and the 5 hr duration of each visit, we included a phase-curve component in our light-curve modeling to account for the changing visibility of the dayside during the planet's egress and ingress, assuming negligible nightside emissions. Following H. Parviainen et al. (2022), the light curve was modeled as a sine wave between 1 and $1 + F_p$ to account for the phase of the planet's dayside during the visits:

$$F = \frac{F_p}{2}\cos\left(\frac{2\pi t}{P} + \pi\right) + \left(1 + \frac{F_p}{2}\right), \quad (1)$$

where F represents the relative flux of the system, F_p the eclipse depth of the visit, P the orbital period, and t the time. Similarly sinusoidal light curves have been modeled for other super-Earths (e.g., D. Rouan et al. 2011; L. Kreidberg et al. 2019; S. Zieba et al. 2022).

We used a pixel-level decorrelation (PLD) model to account for the systematics associated with sensitivity variation and stellar motion on the detector (D. Deming et al. 2015). The analysis was performed by binning the data into 20 s intervals. Two systematic models were implemented on top of the PLD to account for the effects of drift and test for variation: one with a second-order logarithmic ramp in time, and one with an exponential-linear ramp in time (e.g., E. M. May et al. 2022). However, by cutting off the first 45 minutes of each data set, we found that the systematic drift was effectively removed, and subsequent analyses showed that the three systematic models produced results consistent with one another (Figure 1). As such, we used a model with no systematic ramp to reduce the

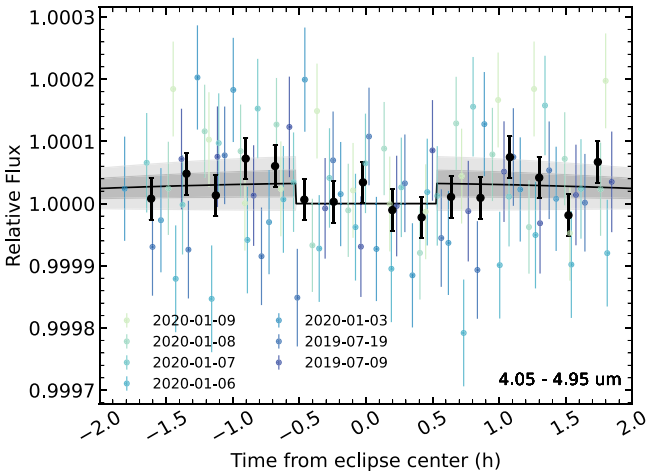

Figure 2. Best-fitting white-light curve from the analysis of the seven eclipses of TOI-431 b with Spitzer Channel 2. The eclipse light curve generated from the average eclipse depth of 33 ppm is shown in the black line, with $\pm1\sigma$ and $\pm2\sigma$ ranges shown in gray. The blue circles represent the individual systematics-corrected observations and their associated error bars. The Spitzer data points are binned to 8.33 minutes intervals, and the bold black points represent the combination of all the data binned by groups of 250 points. The first and last 45 minutes of each data set have been removed.

overall complexity of the model and avoid overfitting for a limited drift.

Using the methodology outlined above, we perform our ExoTEP analysis on all seven visits fitting for the eclipse depth, photometric scatter, and PLD coefficients in each visit. From our MCMC analysis of the light curve, we calculate the weighted average across all seven visits and measure a marginal eclipse depth of 33 ± 22 ppm for TOI-431 b in the 4.5 μm Spitzer channel (Figure 2).

To ensure the robustness of our measurement, we also conducted a quick, independent analysis also using PLD. In this analysis, we first calculated the mean of each stack of 64 IRAC2 subarray frames, resulting in 689 mean frames for each of the seven Spitzer Astronomical Observation Requests (AORs). We then extracted time series from each of the central 9 pixels, and constructed normalized vectors v_{ij} by dividing by the sum at each time step. To capture higher-order PLD effects, we also included a second set of vectors corresponding to v_{ij}^2, as well as a set of seven linear functions in time (within each AOR) to remove any long-term drifts. We then calculated the coefficients of all of these systematics vectors using linear least squares, using only the out-of-eclipse data. After normalizing the photometry by our optimal light-curve model, we excluded 10 time steps as outliers because their residuals were discrepant by $>5\sigma$. Finally, we use the average and standard error on the mean of the remaining points within and outside of the expected eclipse window to calculate the eclipse depth and its uncertainty. This simple analysis yields an eclipse depth of 28 ± 20 ppm, in excellent agreement with the ExoTEP result.

Assuming the planet radiates as a blackbody, we measured the dayside brightness temperature T_p at 4.5 μm to be 1520^{+360}_{-390} K by inverting the following equation:

$$F_{p,\mathrm{avg}} = \frac{\pi R_p^2 B_{4.5\ \mu\mathrm{m}}(T_p)}{\pi R_s^2 F_{s,4.5\ \mu\mathrm{m}}}, \tag{2}$$

where R_p and R_s represent the radius of the planet and star, respectively, $B_{4.5\ \mu\mathrm{m}}(T_p)$ is the blackbody spectrum of the planet at a temperature T_p and wavelength $\lambda = 4.5\ \mu$m, and $F_{s,4.5\ \mu\mathrm{m}}$ is the stellar flux integrated over the Spitzer Channel 2 bandpass, assuming a PHOENIX stellar model for TOI-431 ($T_{\mathrm{eff}} = 4850$ K, $\log g = 4.6$, [M/H] = 0.2; T. O. Husser et al. 2013).

3. Modeling Analysis

Our measured values for the eclipse depth and dayside brightness temperature of TOI-431 b are far lower than anticipated for an atmosphereless bare rock. A low eclipse depth may indicate high levels of heat recirculation around the planet, or a highly reflective surface. In Section 3.1, we investigate the potential heat circulation on TOI-431 b by treating it as a blackbody and investigating its heat redistribution and albedo. Section 3.2 investigates TOI-431 b's surface composition by comparing the measured eclipse depth to emission spectra produced by bare-rock models of different mineralogical compositions. Finally, in Section 3.3, we investigate a number of potential atmospheres on TOI-431 b using the one-dimensional (1D) self-consistent atmosphere modeling framework SCARLET.

3.1. Heat Redistribution around TOI-431 b

3.1.1. Methods

The energy balance and atmospheric circulation of TOI-431 b can be studied by investigating the Bond albedo A_B and heat redistribution factor f. A_B represents the total reflectivity index of the planet integrated over all wavelengths. We assume that the dayside flux of TOI-431 b consists entirely of light from the host star either reflected or reemitted by the surface. This constrains the Bond albedo between 0 (no light is reflected) and 1 (all light is reflected). The heat redistribution factor f represents the efficiency of the heat transport around the planet, particularly through atmospheric circulation, and can range from $1/4$ to $2/3$. A value of $1/4$ indicates that all incident heat is uniformly redistributed around the planet, while a value of $2/3$ indicates that no incident heat is redistributed, such that the planet emits the same amount of energy from its dayside as a bare rock (B. M. S. Hansen 2008; S. Seager 2010). A heat redistribution factor of $1/2$ indicates a special case in which heat is uniformly redistributed, but only on the dayside of the planet (B. M. S. Hansen 2008).

One way to interpret an eclipse measurement in a single spectroscopic band is to assume the planet radiates as a blackbody to probe different combinations of A_B and f (e.g., I. J. M. Crossfield et al. 2022). A_B and f can used to calculate the planet's dayside equilibrium temperature:

$$T_{d,\mathrm{eq}} = T_s \sqrt{\frac{R_s}{a}} (1 - A_B)^{\frac{1}{4}} f^{\frac{1}{4}}. \tag{3}$$

Using this equation, we can constrain the values of A_B and f that reproduce the measured dayside brightness temperature of TOI-431 b.

3.1.2. Results

The two-dimensional (2D) posterior constraining A_B and f suggests that a dark bare-rock scenario is disfavored for TOI-431 b (Figure 3). Although much of the joint posterior is within 1σ of our measured brightness temperature, two sections of the

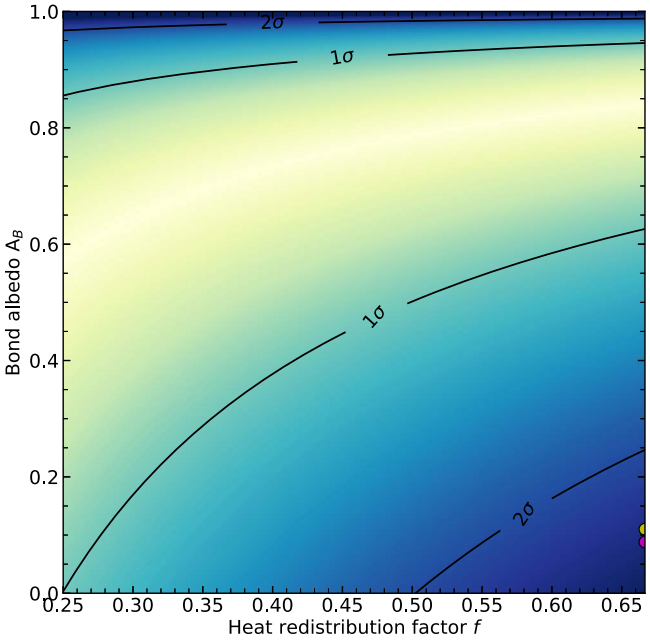

Figure 3. Joint posterior distribution of the Bond albedo A_B (vertical axis) and heat redistribution factor f (horizontal axis) assuming TOI-431 b radiates as blackbody at its 4.5 μm brightness temperature of 1520 K. The 2D posterior is shown using colored shading, where darker regions indicate lower probabilities. The 1σ and 2σ regions are indicated by the black contour lines. The approximate values for the Moon and Mercury are shown in yellow and magenta at the bottom right, respectively.

posterior are disfavored. High Bond albedos ($A_B \lessapprox 1$) are disfavored for all values of f, indicating that an exotic, ultrareflective surface composition is unlikely. More importantly, the region that gives the highest dayside temperature ($A_B = 0$, $f = 2/3$) is disfavored at $>2\sigma$. Airless bodies tend to fall within this regime of minimal heat redistribution and low reflectance (e.g., J. H. Madden & L. Kaltenegger 2018). In our own solar system, airless rocky bodies are generally quite dark, with Bond albedoes of 0.11 for the Moon and 0.088 for Mercury (A. Mallama 2017).

Despite our inferences, much of the parameter space remains unconstrained. First, planets with zero heat redistribution but relatively high Bond albedos are within the 1σ range, indicating that a reflective bare-rock model may be consistent with our observations. Although surface compositions with high Bond albedos are not impossible (see Section 3.2; M. Hammond et al. 2025), high values of A_B are often associated with the presence of clouds (M. Mansfield et al. 2019). Second, the Bond albedo is largely unconstrained for models with smaller values of f, and thus for models with atmospheric heat recirculation. A_B varies heavily between rocky bodies with atmospheres in our own solar system, with 0.25 for Mars and 0.76 for Venus (R. Haus et al. 2016). However, the somewhat unconstrained nature of the heat redistribution factor and the Bond albedo is not surprising, as the two parameters are strongly correlated, as shown in Equation (3). For example, increasing the heat redistribution factor has the same impact on $T_{d,\mathrm{eq}}$ as decreasing A_B.

3.2. Bare-rock Emission Spectra

3.2.1. Methods

We simulated a number of bare-rock emission spectra using the wavelength-dependent albedos of various mineralogical surfaces from R. Hu et al. (2012), who used emissivity measurements of rock samples to calculate the infrared spectra of each surface type (M. B. Wyatt et al. 2001; R. N. Clark et al. 2007; L. Cheek et al. 2009). These models assume an airless environment and one of five surface types: ultramafic, basaltic, feldspathic, iron-oxidized, and metal-rich. These different surface compositions are indicative of different formation histories and chemical abundances (R. Hu et al. 2012; M. Mansfield et al. 2019; M. Zhang et al. 2024). Magnesium-rich ultramafic rocks were common on primordial Earth and Mars, and are formed by the partial melting of rock (T. L. Grove & S. W. Parman 2004). Basaltic crusts associated with volcanism are abundant on the Earth and Moon today. Feldspathic crusts formed by the crystallization of magma oceans are present in the lunar highlands, while iron oxides associated with space weathering widely populate Mars. The metal-rich (pyrite) crust has no known counterpart in our solar system.

The distribution of stellar flux incident on orbiting planets is nonuniform; for an atmosphereless bare rock, the temperature peaks at the substellar point and decreases as we approach the terminator line (B. M. S. Hansen 2008). Our bare-rock model accounts for the nonuniform temperature gradient on the planet's dayside by separating the hemisphere into a large number of rings, with each ring at an angle θ away from the substellar point. The radiance of each ring is then calculated using the emissivities of the surface composition such that the sum of the reflected and thermal emission from each ring is equal to the incident net flux from the host star onto the annular section (C. Monaghan et al. 2025, in preparation).

3.2.2. Results

The nonreflective bare-rock scenarios are inconsistent to 1σ with the measured eclipse depth at 4.5 μm (Figure 4). The ultramafic and feldspathic models are tenuously consistent with the data at the $\leqslant 1.25\sigma$ level, while the remaining models are inconsistent to the data at the $>1.8\sigma$ level. The dark bare-rock scenario is ruled out at 2.5σ. Ultramafic and feldspathic surfaces are highly reflective in the Spitzer NRS2 bandpass ($A_B \geqslant 0.4$). Our constraints on A_B and f for TOI-431 b indicate that a high Bond albedo is required for a planet with minimal heat redistribution (Figure 3). A feldspathic surface composition may be unsuitable for TOI-431 b as feldspar-rich surfaces are less likely to form on Earth-sized planets (L. T. Elkins-Tanton 2012). However, the high temperatures on TOI-431 b may result in a partially molten surface (see discussion below), and as such may produce a surface rich in ultramafic rock. The potential for an ultramafic surface on TOI-431 b is of particular note, as the high albedo of ultramafic surfaces may lead to false positives for atmospheric detection, particularly around M dwarf stars (M. Mansfield et al. 2019).

A number of factors may affect the reflectivity of different surface compositions. Surface texture, chemical contaminants, and space weathering are all known to lower the Bond albedo of airless bodies (R. Brunetto et al. 2015; X. Dumusque et al. 2019; M. Mansfield et al. 2019; X. Lyu et al. 2024; K. Paragas et al. 2025). However, a number of factors may result in a high-albedo surface without an atmospheric presence (e.g., M. Mansfield et al. 2019). Most notably, at higher surface temperatures, the partial devolatization of rock may form a highly reflective corundum surface composed of calcium and aluminum (E. S. Kite et al. 2016). The rate of devolatization

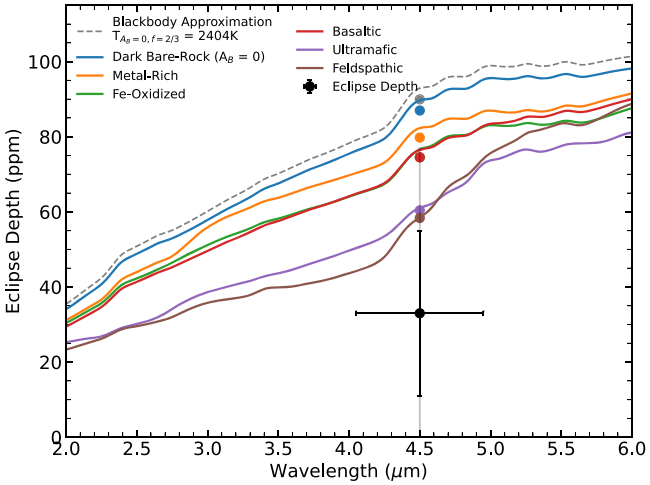

Figure 4. Eclipse depth of TOI-431 b at 4.5 μm compared to a suite of atmosphereless emission spectra from different mineralogical surface models, assuming a PHOENIX stellar model. The black dot represents the measured eclipse depth with the associated $\pm1\sigma$ and $\pm2\sigma$ error bars shown in black and gray, respectively. The colored lines represent the emission spectra of difference surface compositions assuming a nonuniform temperature gradient on the planet's surface. Colored circles represent the models integrated over the IRAC2 bandpass between 4.05 and 4.95 μm. A blackbody model with a uniform dayside temperature is shown for comparison, indicating the difference between itself and the more accurate dark bare-rock model in blue.

becomes notable above 1250 K, and thus hotter regions of TOI-431 b may be affected near the substellar point (M. Mansfield et al. 2019).

Another notable complication we ignore in our bare-rock models is that the emission and reflection spectra of different mineralogical compositions is dependent on temperature (e.g., J. Helbert et al. 2013; S. Ferrari et al. 2020; G. Poggiali et al. 2021; A. H. Treiman et al. 2021). As such, the laboratory reflectance of each composition tested may not accurately describe the conditions on TOI-431 b. Furthermore, TOI-431 b is potentially hot enough to melt components of its surface. Assuming zero heat recirculation and zero reflectance, the maximum dayside temperature of TOI-431 b is ~2400 K as calculated by Equation (3). For reference, silicate rocks start melting at 850K, and all silicate rocks are completely molten by ~1500 K (e.g., F. K. Lutgens et al. 2017). At our measured dayside brightness temperature of 1520 K, components of TOI-431 b's surface may be liquefied. Molten surfaces have different spectral properties from their solid counterparts, but are expected to maintain low albedos of $\leqslant$0.1 (Z. Essack et al. 2020). It is possible that a combination of molten and devolatized rock is present on the surface of TOI-431 b, leading to a nonuniform albedo across the planet's surface.

3.3. SCARLET Atmosphere Models

3.3.1. Methods

We used the SCARLET atmosphere modeling framework to generate a suite of 1D self-consistent atmosphere models of TOI-431 b and compare the model emission spectra to the Spitzer eclipse measurements (e.g., B. Benneke & S. Seager 2012, 2013; B. Benneke 2015; B. Benneke et al. 2019b, 2019a, 2024; S. Pelletier et al. 2021, 2025; P.-A. Roy et al. 2022, 2023; L. Bazinet et al. 2024; C. Piaulet-Ghorayeb et al. 2024). We used the framework to generate nongray models of TOI-431 b assuming a well-mixed composition. The

Table 3
Summary of Atmospheric Models Shown in Figure 5 as Computed by SCARLET, Alongside the Associated Source for Each

Model	pCloud (bar)	Composition (Abundance)	References
Reduced magma ocean	1	H_2: 42% CO: 42% N_2: 15% H_2O: 1%	(1)
Neutral magma ocean	1	CO: 35% CO_2: 30% N_2: 30% H_2O: 4% H_2: 1%	(1)
Reduced rock vapor	10^{-4}	SiO: 46.4% Mg: 28.2% Fe: 25.1% Si: 0.1% O: 0.1% Trace SiO_2, MgO, FeO	(2)
Oxidized rock vapor	10^{-4}	O: 74.6% O_2: 25.1% Fe: 0.01% FeO: 0.01% SiO: 0.01% Mg: 0.01%	(2)

Note. "Trace" implies an abundance of 0.001%.
References. (1) M. Maurice et al. (2024), (2) F. L. Seidler et al. (2024).

wavelength-dependent models calculate the chemical composition of the planet by solving for hydrostatic equilibrium and radiative transfer iteratively to produce a theoretical temperature–pressure profile of the planet. Once the model converges to a stable temperature profile and chemistry, the associated emission spectrum from the secondary eclipse is computed. The stellar spectrum is accounted for in the model using the same PHOENIX stellar emission spectrum described earlier.

Our suite of models studies a variety of atmospheric compositions that may be generated on TOI-431 b. We test two atmospheres produced by volatile magma oceans, and two metal-rich rock vapor atmospheres. The exact compositions of the models simulated are shown in Table 3.

The chemical abundances of the magma outgassed atmospheres were approximated from Figure 3 of M. Maurice et al. (2024), which represents the compositions produced by lava oceans of different oxidation states. Although such compositions represent a primordial magma ocean during the early lifetime of an exoplanet, they may approximate the chemistry associated with a permanent magma ocean rich with volatiles. We model the atmospheres produced on a $3M_\oplus$ planet by a heavily reduced magma ($\Delta\mathrm{IW} = -5$) and by a neutral magma (Earth-like, $\Delta\mathrm{IW} = 0$), assuming both oceans are 0.5 times the planetary silicate mass.

We test the neutral magma ocean model at two levels of heat redistribution: one with full recirculation to the nightside of the planet ($f = \frac{1}{4}$), and one with uniform recirculation on the dayside only ($f = \frac{1}{2}$). The inclusion of a model without nightside atmospheric circulation is done to simulate a planet where the atmosphere condensates or solidifies on the nightside due to the colder temperatures, and to showcase that a thick, entirely redistributive atmosphere may not be required to produce the observed eclipse depth of TOI-431 b (e.g., V. Parmentier et al. 2018; D. Ehrenreich et al. 2020).

The chemical abundances of the rock vapor atmospheres were approximated from Figure 6 of F. L. Seidler et al. (2024), which represents the mineral atmospheres produced by a silicate-rich magma using a bulk silicate Earth-like mantle composition model. To specify the abundances of the well-

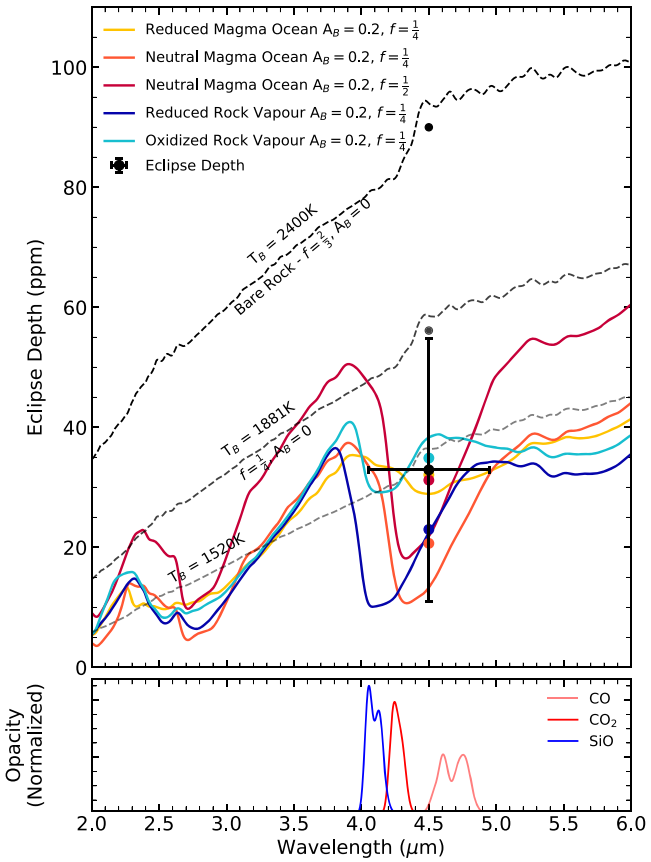

Figure 5. Eclipse depth of TOI-431 b at 4.5 μm compared to a suite of theoretical emission spectra produced by SCARLET. The colored lines represent the five atmospheric models simulated by SCARLET using a nongray temperature profile and a well-mixed composition. The dashed gray lines show the blackbody eclipse spectra corresponding to different combinations of f and A_B at uniform dayside temperatures. The black dot represents the measured eclipse depth, with the associated $\pm 1\sigma$ error bars. Colored circles represent the models integrated over the IRAC2 bandpass between 4.05 and 4.95 μm. The exact compositions of the atmospheric models are shown in Table 3. Normalized opacity bands from dominating molecules in the models (CO, CO_2, and SiO) are shown in the bottom panel.

mixed composition type, we choose to use the mixing ratios simulated at an irradiation temperature of 2000 K and 10^{-4} bars of pressure for a highly oxidized environment ($\Delta\mathrm{IW} = 4$) and a highly reduced state ($\Delta\mathrm{IW} = -4$).

3.3.2. Results

The model emission spectra for the rock vapor and magma ocean atmospheres agree well with our measured eclipse depth within 1σ (Figure 5). Most notably, the neutral magma ocean with uniform dayside redistribution ($f = \frac{1}{2}$) is shown to be consistent due to the large absorption band at $\sim$4.5 μm, despite the lack of atmospheric recirculation to the nightside of the planet. The blackbody model at $f = \frac{1}{4}$, $A_B = 0$ is shown to be tenuously consistent at $\sim 1\sigma$.

There are a number of potential caveats to our SCARLET models. The presence of clouds, winds, and photochemistry may all affect the temperature–pressure profile and composition of TOI-431 b in complex ways. A number of cloud species have condensation temperatures around the dayside brightness temperature of TOI-431 b, and as such could be present on the planet (K. Lodders 2002; H. R. Wakeford et al. 2016). We further note that the chosen chemical abundances simulated in our well-mixed compositions are only approximations. M. Maurice et al. (2024) simulates the volatile-rich atmospheres at a much higher pressure than those expected for TOI-431 b, while the mixing ratios simulated by F. L. Seidler et al. (2024) are sensitive to a range of potential atmospheric pressures. These models also generate different temperature–pressure profiles than the ones generated by SCARLET. The rock vapor profiles generated by F. L. Seidler et al. (2024) in particular are inverted due to the presence of other optical absorbers in the simulated atmospheres. These potential caveats are unlikely to affect our results due to the large uncertainties in our measured eclipse depth. The models should remain consistent under small modifications to the chemical abundances or temperature profile.

4. Discussion

Our combined atmospheric analysis of TOI-431 b disfavors a low-albedo bare-rock composition at 2.5σ, hinting toward either an atmospheric presence or a highly reflective bare-rock surface. However, probing the composition of a planetary atmosphere from an eclipse depth in a single wavelength regime does not place stringent constraints on the planet's composition. We discuss the results of our data reduction and analysis below. In Section 4.1, we discuss the significance of TOI-431 b's low eclipse depth. We then consider the potential atmospheric scenarios that may produce a shallow eclipse depth in Section 4.2. Finally, in Section 4.3, we discuss the potential for follow-up observations of TOI-431 b, and what they may reveal regarding the nature of the planet.

4.1. Interpreting the Absence of a Deep Eclipse

The occultation depth of 33 ± 22 ppm measured for TOI-431 b is not a significant detection (1.5σ). However, the absence of a deep eclipse disfavors the bare-rock scenario, which suggests an eclipse depth of $\sim$90 ppm in the IRAC2 bandpass of Spitzer. If the eclipse depth of the planet were this deep, our 22 ppm precision would have resulted in a detection at $>4\sigma$. Thus, we have the precision to strongly detect the eclipse of a bare-rock composition.

Another factor to consider is the possibility that the occultation events were not observed during each Spitzer visit due to a highly eccentric orbit. An eccentric orbit for TOI-431 b would be unexpected due to its proximity to the host star. Closely orbiting planets like TOI-431 b generally have negligible eccentricities due to tidal circularization (e.g., F. A. Rasio et al. 1996; G. W. Marcy et al. 1997; A. Rodríguez et al. 2011). We estimate the circularization timescale of TOI-431 b using Equation (2) provided by B. Jackson et al. (2008). Depending on TOI-431 b's Love number k_2 and quality factor Q, the circularization timescale is $\leqslant$6 Myr using Jupiter's values of k_2 and Q, which likely underestimate the tidal forces exerted on TOI-431 b (B. Jackson et al. 2008; V. Lainey 2016). Comparing this timescale to the estimated age of the TOI-431 system (1.9 Gyr) indicates that the orbit of TOI-431 b is highly unlikely to be eccentric, in agreement with the result based on radial velocity data (A. Osborn et al. 2021).

To further ensure the occultation events were observed in each Spitzer visit, we estimated the maximum phase offset of TOI-431 b's eclipse assuming an eccentric orbit. In the discovery of TOI-431 b, A. Osborn et al. (2021) measure a 95% confidence interval from 0 to 0.28 for the planet's

eccentricity. The phase of a secondary-eclipse event can be calculated with

$$\text{phase} = \frac{1}{2} + \frac{2}{\pi} e \cos(\omega), \quad (4)$$

where e is the eccentricity and ω the argument of periastron (J. N. Winn 2014). With this equation, we measure a maximum timing offset from half-phase of 125 minutes, assuming $e = 0.28$ and $\omega = 0$. With each Spitzer visit centered on half-phase and lasting 5.24 hr, the occultation events would be observed at least partially for all observations.

4.2. Potential Atmospheric Scenarios

A significant atmosphere on TOI-431 b would be difficult to maintain for a long lifetime. XUV irradiation from its host star is theorized to drive atmospheric photoevaporative escape at rates of 10^6–10^8 kg s^{-1}, far higher than the CO_2 outgassing rate of Earth (T. Plank & C. E. Manning 2019; G. W. King et al. 2024; X. Jiang et al. 2025). Although a rapidly outgassing magma ocean may exceed the mass-loss rate, the outgassing rate on such planets is dependent on a number of factors, and is difficult to constrain (e.g., C. Dorn et al. 2018; R. J. Spaargaren et al. 2020; P. Baumeister et al. 2023).

The 'cosmic shoreline' theory proposes that a planet's ability to retain an atmosphere is based on the predicted escape velocity and XUV irradiation (K. J. Zahnle & D. C. Catling 2017). TOI-431 b is expected to receive $\sim 7 \times 10^4$–9×10^4 erg s^{-1} cm^2 of XUV irradiation, placing it well above the shoreline (G. W. King et al. 2024; X. Jiang et al. 2025). However, 55 Cnc e is similarly placed well above the cosmic shoreline, despite evidence to suggest the planet hosts a volatile-rich atmosphere (R. Hu et al. 2024; J. A. Patel et al. 2024). Furthermore, TOI-431 b is also exposed to high levels of XUV irradiation, and suffers atmospheric loss at a rate of 10^7 kg s^{-1}(K. Heng 2023). As such, the planet may instead host a transient atmosphere, which could cause the apparent variability seen in phase-curve observations (K. Heng 2023; J. A. Patel et al. 2024). Further evidence of flux variability of TOI-431 b in the optical and infrared regimes would be necessary to determine the presence of transient outgassing.

4.3. Follow-up Observations

Follow-up studies of TOI-431 b's emission spectrum are necessary to confirm the low occultation depth and investigate an atmospheric presence. A number of spectral features may be used to analyze the volatile content in spectroscopic analysis. A volatile-rich atmosphere with CO/CO_2 can be identified by its large absorption between 4–5 μm, while a mineral-rich atmosphere may be identified using the SiO feature visible at 4.2 μm (Figure 5). Spectral features may be identified at longer wavelengths, including MgO at 6 μm, SiO at 9 μm, and CO_2 at 15 μm (e.g., G. H. Rieke et al. 2015; F. L. Seidler et al. 2024).

Identifying molecular signatures on TOI-431 b requires the use of spectroscopy, which is readily achieved using a number of instruments on the JWST. Comparing the observed eclipse depth within these wavelength regimes may constrain the bulk volatile content and oxidation of TOI-431 b's atmosphere, and may probe the temperature–pressure profile of the planet itself. Further information regarding the planet's energy budget, heat redistribution, and 2D structure may be inferred through phase-curve observations, which could also be used to analyze the redistribution of heat around the planet.

If an atmosphere is present on TOI-431 b, constraining its composition would significantly further our understanding of the potential atmospheres a planet can retain under high irradiation. The models simulated above were chosen due to their similarities to atmospheres proposed for other rocky exoplanets. Recent observations of the emission spectra of 55 Cnc e may indicate the presence of a similarly volatile atmosphere composed of CO or CO_2 sustained by the outgassing of a magma ocean (R. Hu et al. 2024; J. A. Patel et al. 2024). Furthermore, rock vapor atmospheres have previously been proposed for other hot USPs, including K2-141 b and 55 Cnc e (S. Zieba et al. 2022; K. C. Rasmussen et al. 2023). The prevalence and nature of rock vapor atmospheres will be further studied as part of GO 4818 (PI: Mansfield).

5. TOI-431 b in Context

TOI-431 b joins a growing list of rocky planets ($\leqslant 2R_\oplus$) with measured infrared thermal emissions. The notably low dayside emission interrupts a trend first noted by I. J. M. Crossfield et al. (2022) of smaller planets having temperatures consistent with bare-rock models (e.g., T. P. Greene et al. 2023; S. Zieba et al. 2023; E. Ducrot et al. 2024; R. Luque et al. 2024; M. W. Mansfield et al. 2024; P. Wachiraphan et al. 2024; Q. Xue et al. 2024; M. Zhang et al. 2024). TOI-431 b is now the fourth rocky exoplanet with thermal emissions showing some evidence for heat redistribution, alongside 55 Cnc e, K2-141 b, and LHS 1478 b (S. Zieba et al. 2022; P. C. August et al. 2025; R. Hu et al. 2024). While LHS 1478 b orbits a relatively cool M dwarf, the other three planets are subject to the highest levels of irradiation from their host stars when compared to other planets with thermal emission observations. This may indicate that highly irradiated planets outgas secondary atmospheres more efficiently. Furthermore, these three planets are known to orbit relatively hot stars: 55 Cnc e orbits a G star, while K2-141 b and TOI-431 b both orbit K stars. The potential for atmospheric retention may therefore be impacted by the host star itself. Many planets observed in the infrared regime through secondary eclipses orbit M stars. M dwarfs are generally active; stellar winds, coronal mass ejections, and XUV irradiation may contribute to the atmospheric erosion of orbiting bodies (L. Mignon et al. 2023). However, the thermal emission measured from the super-Earth LHS 1478 b indicates a brightness temperature inconsistent with the bare-rock hypothesis, despite the planet orbiting an M dwarf star (P. C. August et al. 2025). It should be noted that the results from LHS 1478 b are based on a single eclipse visit.

Further study is required to fully understand the presence and composition of rocky planet atmospheres. The trends discussed above are tenuous at best, largely due to the lack of data points necessary for reliable conclusions to be made. A variety of factors may play a role in retaining the atmospheres of rocky bodies, including stellar type and planetary radius. Future and ongoing observations by the JWST will expand the scope of research into rocky planet atmospheres through secondary-eclipse and phase-curve observations. GO 4818 (PI: Mansfield) will investigate the formation and properties of silicate atmospheres using MIRI/LRS eclipse observations of the potential lava worlds GJ 9827 b, HD 20329 b, TOI-1416 b, TOI-500 b, TOI-1442 b, TOI-561 b, TOI-1075 b, TOI-1807 b,

HD 3167 b, and TOI-431 b. The atmospheres of rocky M dwarf exoplanets will also be investigated as part of the proposed 500 hr JWST DDT program, which has so far been confirmed to observe LTT 1445A c and GJ 3929 b (S. Redfield et al. 2024). Among these larger surveys, the JWST will also observe TOI-2445A b (GO 3784), TOI-4481 b (GO 4931), and LP-781-18 d (GO 6457).

6. Conclusion

TOI-431 b is among the first terrestrial planets with infrared thermal emission observations to show a notably low eclipse depth. Our modeling of the planet's composition disfavors a low-albedo bare-rock scenario, and instead suggests the presence of an atmosphere potentially fueled by the outgassing of a magma ocean. Alternatively, the planet's low eclipse depth may be produced by a bare rock whose surface is highly reflective. Constraining the exact composition of the planet, however, requires further study with modern instrumentation, and it remains to be understood how an atmospheric presence on TOI-431 b could be maintained under the intense XUV radiation from its host star. Future observations of TOI-431 b offer the opportunity to further investigate the nature of this planet and further probe its surface and atmospheric composition. We encourage further research into the infrared emission spectra of rocky exoplanets to understand their compositions and potential for atmospheric retention.

Acknowledgments

This work is based on observations made with the Spitzer Space Telescope, which was operated by the Jet Propulsion Laboratory, California Institute of Technology, under a contract with NASA. C.M. and P.-A.R. acknowledge financial support from the University of Montreal, and C.M. further acknowledges financial support from Jean-Marc Lauzon. B.B., P.-A.R., and C.M. acknowledge financial support from the Natural Sciences and Engineering Research Council (NSERC) of Canada. C.P.-G acknowledges support from the NSERC Vanier scholarship, and the Trottier Family Foundation. C.P.-G also acknowledges support from the E. Margaret Burbidge Prize Postdoctoral Fellowship from the Brinson Foundation. This work was made with the support of the Institut Trottier de Recherche sur les Exoplanetes (iREx).

ORCID iDs

Christopher Monaghan https://orcid.org/0009-0005-9152-9480
Pierre-Alexis Roy https://orcid.org/0000-0001-6809-3520
Björn Benneke https://orcid.org/0000-0001-5578-1498
Louis-Philippe Coulombe https://orcid.org/0000-0002-2195-735X
Caroline Piaulet-Ghorayeb https://orcid.org/0000-0002-2875-917X
Laura Kreidberg https://orcid.org/0000-0003-0514-1147
Courtney D. Dressing https://orcid.org/0000-0001-8189-0233
Stephen R. Kane https://orcid.org/0000-0002-7084-0529
Diana Dragomir https://orcid.org/0000-0003-2313-467X
Michael W. Werner https://orcid.org/0000-0003-4990-189X
Vivien Parmentier https://orcid.org/0000-0001-9521-6258
Jessie L. Christiansen https://orcid.org/0000-0002-8035-4778
Farisa Y. Morales https://orcid.org/0000-0001-9414-3851
David Berardo https://orcid.org/0000-0001-6298-412X
Varoujan Gorjian https://orcid.org/0000-0002-8990-2101

References

Alonso, R. 2018, in Handbook of Exoplanets, ed. H. J. Deeg & J. A. Belmonte (New York: Springer), 40
August, P. C., Buchhave, L. A., Diamond-Lowe, H., et al. 2025, A&A, 695, A171
Baumeister, P., Tosi, N., Brachmann, C., Grenfell, J. L., & Noack, L. 2023, A&A, 675, A122
Bazinet, L., Pelletier, S., Benneke, B., Salinas, R., & Mace, G. N. 2024, AJ, 167, 206
Benneke, B. 2015, arXiv:1504.07655
Benneke, B., Knutson, H. A., Lothringer, J., et al. 2019a, NatAs, 3, 813
Benneke, B., Roy, P.-A., Coulombe, L.-P., et al. 2024, arXiv:2403.03325
Benneke, B., & Seager, S. 2012, ApJ, 753, 100
Benneke, B., & Seager, S. 2013, ApJ, 778, 153
Benneke, B., Werner, M., Petigura, E., et al. 2017, ApJ, 834, 187
Benneke, B., Wong, I., Piaulet, C., et al. 2019b, ApJL, 887, L14
Brunetto, R., Loeffler, M. J., Nesvorný, D., Sasaki, S., & Strazzulla, G. 2015, in Asteroids IV, ed. P. Michel, F. E. DeMeo, & W. F. Bottke (Tucson, AZ: Univ. Arizona Press), 597
Cheek, L., Pieters, C., Dyar, M., & Milam, K. 2009, LPSC, 40, 1928
Clark, R. N., Swayze, G. A., Wise, R. A., et al. 2007, USGS Digital Spectral Library splib06a Technical Report, US Geological Survey
Crossfield, I., Werner, M., Dragomir, D., et al. 2018, Spitzer Transits of New TESS Planets 14084, Spitzer Proposal
Crossfield, I. J. M., Malik, M., Hill, M. L., et al. 2022, ApJL, 937, L17
Deming, D., Knutson, H., Kammer, J., et al. 2015, ApJ, 805, 132
Demory, B.-O., Gillon, M., Madhusudhan, N., & Queloz, D. 2015, MNRAS, 455, 2018
Dorn, C., Noack, L., & Rozel, A. B. 2018, A&A, 614, A18
Ducrot, E., Lagage, P.-O., Min, M., et al. 2024, NatAs, in press
Dumusque, X., Turner, O., Dorn, C., et al. 2019, A&A, 627, A43
Ehrenreich, D., Lovis, C., Allart, R., et al. 2020, Natur, 580, 597
Elkins-Tanton, L. T. 2012, AREPS, 40, 113
Essack, Z., Seager, S., & Pajusalu, M. 2020, ApJ, 898, 160
Ferrari, S., Maturilli, A., Carli, C., et al. 2020, E&PSL, 534, 116089
Foreman-Mackey, D., Hogg, D. W., Lang, D., & Goodman, J. 2013, PASP, 125, 306
Fulton, B. J., Petigura, E. A., Howard, A. W., et al. 2017, AJ, 154, 109
Ginzburg, S., Schlichting, H. E., & Sari, R. 2016, ApJ, 825, 29
Ginzburg, S., Schlichting, H. E., & Sari, R. 2018, MNRAS, 476, 759
Greene, T. P., Bell, T. J., Ducrot, E., et al. 2023, Natur, 618, 39
Grove, T. L., & Parman, S. W. 2004, E&PSL, 219, 173
Hammond, M., Guimond, C. M., Lichtenberg, T., et al. 2025, ApJL, 978, L40
Hansen, B. M. S. 2008, ApJS, 179, 484
Haus, R., Kappel, D., Tellmann, S., et al. 2016, Icar, 272, 178
Helbert, J., Nestola, F., Ferrari, S., et al. 2013, E&PSL, 371, 252
Heng, K. 2023, ApJL, 956, L20
Hord, B. J., Kempton, E. M. R., Mikal-Evans, T., et al. 2024, AJ, 167, 233
Hu, R., Bello-Arufe, A., Zhang, M., et al. 2024, Natur, 630, 609
Hu, R., Ehlmann, B. L., & Seager, S. 2012, ApJ, 752, 7
Husser, T. O., Wende-von Berg, S., Dreizler, S., et al. 2013, A&A, 553, A6
Jackson, B., Greenberg, R., & Barnes, R. 2008, ApJ, 678, 1396
Jiang, X., Jiang, J. H., Burn, R., & Zhu, Z.-H. 2025, ApJ, 980, 175
Kammer, J. A., Knutson, H. A., Line, M. R., et al. 2015, ApJ, 810, 118
Kane, S. R., Roettenbacher, R. M., Unterborn, C. T., Foley, B. J., & Hill, M. L. 2020, PSJ, 1, 36
Kempton, E. M.-R., Bean, J. L., Louie, D. R., et al. 2018, PASP, 130, 114401
King, G. W., Corrales, L. R., Fernández, J. F., et al. 2024, MNRAS, 530, 3500
Kite, E. S., & Barnett, M. N. 2020, PNAS, 117, 18264
Kite, E. S., Fegley, Bruce, J., Schaefer, L., & Gaidos, E. 2016, ApJ, 828, 80
Koll, D. D. B., Malik, M., Mansfield, M., et al. 2019, ApJ, 886, 140
Kreidberg, L., Koll, D. D. B., Morley, C., et al. 2019, Natur, 573, 87
Kubyshkina, D. 2024, arXiv:2402.13931
Lainey, V. 2016, CeMDA, 126, 145
Liggins, P., Jordan, S., Rimmer, P. B., & Shorttle, O. 2022, JGRE, 127, e2021JE007123
Liggins, P., Jordan, S., Rimmer, P. B., & Shorttle, O. 2023, JGRE, 128, e2022JE007528

Lodders, K. 2002, ApJ, 577, 974
Lopez, E. D. 2017, MNRAS, 472, 245
Luque, R., Coy, B. P., Xue, Q., et al. 2024, arXiv:2412.03411
Lutgens, F. K., Tarbuck, E. J., & Tasa, D. 2017, Essentials of Geology (13th ed.; London: Pearson) 978-0134446622
Lyu, X., Koll, D. D. B., Cowan, N. B., et al. 2024, ApJ, 964, 152
Madden, J. H., & Kaltenegger, L. 2018, AsBio, 18, 1559
Mallama, A. 2017, arXiv:1703.02670
Mansfield, M., Kite, E. S., Hu, R., et al. 2019, ApJ, 886, 141
Mansfield, M. W., Xue, Q., Zhang, M., et al. 2024, ApJL, 975, L22
Marcy, G. W., Butler, R. P., Williams, E., et al. 1997, ApJ, 481, 926
Maurice, M., Dasgupta, R., & Hassanzadeh, P. 2024, A&A, 688, A47
May, E. M., Stevenson, K. B., Bean, J. L., et al. 2022, AJ, 163, 256
Mignon, L., Meunier, N., Delfosse, X., et al. 2023, A&A, 675, A168
Osborn, A., Armstrong, D. J., Cale, B., et al. 2021, MNRAS, 507, 2782
Paragas, K., Knutson, H. A., Hu, R., et al. 2025, ApJ, 981, 130
Parmentier, V., Line, M. R., Bean, J. L., et al. 2018, A&A, 617, A110
Parviainen, H., Wilson, T. G., Lendl, M., et al. 2022, A&A, 668, A93
Patel, J. A., Brandeker, A., Kitzmann, D., et al. 2024, A&A, 690, A159
Pelletier, S., Benneke, B., Chachan, Y., et al. 2025, AJ, 169, 10
Pelletier, S., Benneke, B., Darveau-Bernier, A., et al. 2021, AJ, 162, 73
Pepe, F., Mayor, M., Rupprecht, G., et al. 2002, Msngr, 110, 9
Piaulet-Ghorayeb, C., Benneke, B., Radica, M., et al. 2024, ApJL, 974, L10
Plank, T., & Manning, C. E. 2019, Natur, 574, 343
Poggiali, G., Brucato, J. R., Dotto, E., et al. 2021, Icar, 354, 114040
Rasio, F. A., Tout, C. A., Lubow, S. H., & Livio, M. 1996, ApJ, 470, 1187
Rasmussen, K. C., Currie, M. H., Hagee, C., et al. 2023, AJ, 166, 155
Redfield, S., Batalha, N., Benneke, B., et al. 2024, arXiv:2404.02932
Ricker, G. R., Winn, J. N., Vanderspek, R., et al. 2014, JATIS, 1, 014003
Rieke, G. H., Wright, G. S., Böker, T., et al. 2015, PASP, 127, 584
Rodríguez, A., Ferraz-Mello, S., Michtchenko, T. A., Beaugé, C., & Miloni, O. 2011, MNRAS, 415, 2349
Rouan, D., Deeg, H. J., Demangeon, O., et al. 2011, ApJ, 741, L30
Roy, P.-A., Benneke, B., Piaulet, C., et al. 2022, ApJ, 941, 89
Roy, P.-A., Benneke, B., Piaulet, C., et al. 2023, ApJL, 954, L52
Sanchis-Ojeda, R., Rappaport, S., Winn, J. N., et al. 2014, ApJ, 787, 47
Schaefer, L., & Fegley, B. 2009, ApJ, 703, L113
Seager, S. 2010, Exoplanet Atmospheres: Physical Processes (Princeton, NJ: Princeton Univ. Press)
Seidler, F. L., Sossi, P. A., & Grimm, S. L. 2024, A&A, 691, A159
Spaargaren, R. J., Ballmer, M. D., Bower, D. J., Dorn, C., & Tackley, P. J. 2020, A&A, 643, A44
Tian, M., & Heng, K. 2024, ApJ, 963, 157
Treiman, A. H., Filiberto, J., & Vander Kaaden, K. E. 2021, PSJ, 2, 43
Tsiaras, A., Rocchetto, M., Waldmann, I. P., et al. 2016, ApJ, 820, 99
Unterborn, C. T., Foley, B. J., Desch, S. J., et al. 2022, ApJL, 930, L6
Vogt, S. S., Allen, S. L., Bigelow, B. C., et al. 1994, Proc. SPIE, 2198, 362
Wachiraphan, P., Berta-Thompson, Z. K., Diamond-Lowe, H., et al. 2024, arXiv:2410.10987
Wakeford, H. R., Visscher, C., Lewis, N. K., et al. 2016, MNRAS, 464, 4247
Whittaker, E. A., Malik, M., Ih, J., et al. 2022, AJ, 164, 258
Winn, J. N. 2014, arXiv:1001.2010
Winn, J. N., Sanchis-Ojeda, R., & Rappaport, S. 2018, NewAR, 83, 37
Wordsworth, R., & Kreidberg, L. 2022, ARA&A, 60, 159
Wyatt, M. B., Christensen, P. R., & Taylor, L. A. 2001, JGR, 106, 14711
Xue, Q., Bean, J. L., Zhang, M., et al. 2024, ApJ, 973, L8
Zahnle, K. J., & Catling, D. C. 2017, ApJ, 843, 122
Zhang, M., Hu, R., Inglis, J., et al. 2024, ApJL, 961, L44
Zieba, S., Zilinskas, M., Kreidberg, L., et al. 2022, A&A, 664, A79
Zieba, S., Kreidberg, L., Ducrot, E., et al. 2023, Natur, 620, 746